ORIGINAL ARTICLE

Single toroidal roller burnishing of 2024-T3 Al alloy implemented as mixed burnishing process

G. V. Duncheva[1] · J. T. Maximov[1] · V. P. Dunchev[1] · A. P. Anchev[1] · T. P. Atanasov[1] · Jiri Capek[2]

Abstract

Based on a comprehensive experimental study, single toroidal roller burnishing (STRB) of the 2024-T3 Al alloy can be successfully implemented as a mixed burnishing process. Optimum values of various governing factors provided minimum roughness and significant enhancement of the fatigue life of the treated specimens. With a planned experiment, regression analysis, and optimization procedure based on a genetic algorithm, the optimum factor values were established under a minimum roughness criterion. The derived model predicted a minimum roughness $R_a = 0.074\ \mu m$. The experiment with optimal process parameters provided an average roughness (R_a) of 0.01 μm. STRB under these optimal conditions yields a relatively homogeneous surface in terms of microhardness with a surface microhardness increase coefficient of 37.6%. The parametric study of the residual surface hoop and axial stresses conducted via X-ray stress analysis shows that the STRB with near-optimal process parameters introduces significant residual stresses. STRB of the 2024-T3 Al alloy, implemented as a mixed burnishing process, produces a mirror-finish surface, improves the fatigue life by more than 2000 times, and increases the conventional fatigue limit by 35.1% compared to the reference condition.

Keywords 2024-T3 Al alloy · Single toroidal roller burnishing · Roughness · Microhardness · Residual stresses · Fatigue life enhancement

Abbreviations

CNC	Computer numerical control
HBB	Hydrostatic ball burnishing
LPB	Low plasticity burnishing
MST	Mechanical surface treatment
SRB	Single roller burnishing
STRB	Single toroidal roller burnishing

List of symbols

A_5	Elongation
D	External diameter of the toroidal deforming roller
d	Workpiece (specimen) diameter
f	Feed rate
F_b	Burnishing force
k_{HV}	Surface microhardness increase coefficient
n	Number of passes
N	Number of cycles to failure
r	Radius of the toroid of the toroidal deforming roller
R	Cycle asymmetry coefficient
R_a	Surface roughness
s_i	X-ray elastic constant
v	Burnishing velocity
x_i	Coded variables
$\widetilde{x}_i$	Natural variables
Y_{Ra}	Objective function of the roughness
σ_{-1}	Fatigue limit for symmetrical cycle
σ_u	Ultimate stress
σ_Y	Yield limit
σ_t^{res}	Residual hoop stress
σ_z^{res}	Residual axial stress
ψ	Transverse contraction

✉ G. V. Duncheva
duncheva@tugab.bg

1 Technical University of Gabrovo, 5300 Gabrovo, Bulgaria

2 Czech Technical University in Prague, Prague, Czech Republic

1 Introduction

Modern structural and machine components must operate in conditions of increasing speeds and loads while minimizing their mass and size. High-strength aluminum alloys, including

2024-T3, are appropriate materials because of their high strength to weight ratio, high fatigue resistance, corrosion resistance, and workability. These properties make 2024-T3 aluminum alloy one of the most attractive materials for aircraft, aerospace, and automotive applications and for structural elements in mechanical engineering. For these applications, fatigue strength is crucial for the service life and safety of the components. The fatigue cracks caused by cyclic loading originate mainly in the surface layers, where the largest working stresses occur. Therefore, the operational properties of the structural elements depend on the complex properties of the surface layers, defining the surface integrity (SI). To improve these properties, low roughness, increased microhardness, residual compressive stresses, and modified microstructure in the surface layers are necessary. A cost-effective approach to achieve the desired SI is mechanical surface treatment (MST), which is based on plastic deformation of surface peaks under the conditions of sliding friction or rolling contact between a deforming element and the treated surface. The methods of MST are either dynamic or static (burnishing). Although the dynamic methods were developed first, the burnishing methods have a wider range of applications. Up-to-date classification of the static MST methods is described in [1]. The main feature of MST classification is the type of tangential contact between the deforming element and the treated surface—sliding friction or rolling contact. There are two types of processes with this feature: roller (ball) burnishing and slide (diamond) burnishing.

In general, the burnishing processes with rolling contact have a greater practical application. Ecoroll presents two types of these processes—roller burnishing and deep rolling—according to the desired SI in correlation with the operating behavior [2]. The aim of the roller burnishing process is to achieve a smoothing effect as the roughness is reduced considerably ($R_a \leq 0.2\ \mu m$), and mirror-finish surfaces are achieved. The deep rolling concept is developed for dynamically loaded components. Therefore, the emphasis is on cold work and creation of compressive residual stresses in the surface layers, as the smoothing is an accompanying effect. The roller burnishing process is implemented most often via multiple-roller tools [2]. The deep rolling process is implemented using the following basic methods: hydrostatic ball burnishing (HBB), low plasticity burnishing (LPB), and single roller burnishing (SRB). Although, physically, the LPB corresponds to the hydrostatic ball burnishing, the LPB technique is different in principle. The fundamental goal of LPB is to create a zone of significant compressive residual stresses with minimal cold work and thus minimizing the effect of residual stresses relaxation due to mechanical or thermal overloading. The HBB process effectiveness to improve the obtained roughness, microhardness, and microstructure in rotational and planar components was studied with respect to different materials: AISI 1060 high carbon steel [3, 4],

magnesium alloys [5, 6], 7075-T73 aluminum alloy and Ti-6Al-4V titanium alloys [7], EN AW 2007 aluminum alloy for cases with and without additional vibrations [8], 15-5 PH high alloy steel [9], gamma titanium aluminides [10], and Inconel 718 [11]. Using an experimental design, Yuan et al. investigated the effects of LPB parameters on the surface integrity characteristics of TA2 alloy plates [12].

SRB is implemented via a cylindrical, conical, or toroidal roller. SRB is particularly suitable for finishing rotary elements owing to the following advantages: easy implementation on conventional and CNC lathes; low value for cost/quality ratio; the need for relatively simple devices; ease of control of the process when the deforming force is applied through an elastic system. The SRB process effectiveness with cylindrical rollers for improving the SI of cylindrical specimens was investigated experimentally with different materials: brass [13], mild steel [14], 63400 aluminum alloy [15], 6061 aluminum alloy [16–18], Al-(B4C)$_p$ metal matrix composite [19], and pure aluminum alloyed by copper [20]. Tian and Shin [21] experimentally investigated the laser-assisted burnishing process on annealed and hardened AISI 4140 steel using a roller tool with a conical geometry. Because of the temporary softening of workpiece material prior to burnishing, this hybrid process can produce far better surface finish, higher surface hardness, and similar compressive residual stresses compared to the conventional burnishing. As a whole, the single toroidal roller burnishing (STRB) process has been studied in a limited number of publications [22–25]. A principal scheme of this method, using a toroidal deforming roller, is shown in Fig. 1. Borkar et al. [22] examined the roughness and microhardness in Inconel 718 high-strength alloy as a function of the process parameters. In-depth distribution of residual stresses in railway axles, made of EA4T steel, was studied experimentally by X-ray diffraction and hole drilling in [23]. Dwivedi et al. [24] established that burnished samples of A356/5%SiC metal matrix composite led to improvements
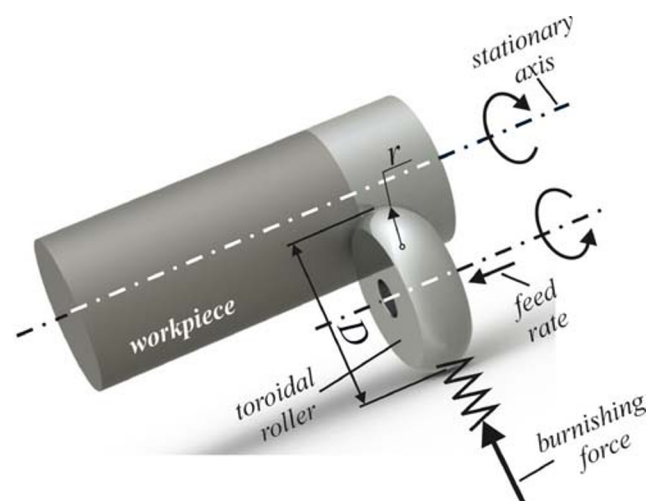

Fig. 1 STRB kinematics

in tensile strength, hardness, and ductility in comparison with unburnished samples. Focusing on the residual stresses, Perenda et al. [25] investigated deep rolling of high-strength TORKA steel torsion bars. Finite element modeling and optimization of the axial residual stress distribution in 2024-T3 Al alloy specimens were presented in [26]. The literature survey shows that there are no experimental studies on the effectiveness of the STRB process to improve SI 2024-T3 Al-alloy components.

Ecoroll classification is based on the depth of the affected layer (the layer of metal with the presence of residual deformations). While, in the roller burnishing process, the depth of the affected layer is insignificant, the deep rolling process affects a much greater depth. The deforming toroidal roller geometry leads to a smaller contact area compared to the cylindrical roller. As a result, with the same burnishing force, the impact is at a greater depth. Therefore, STRB is appropriate for the implementation of the deep rolling concept. The STRB process parameters of interest minimum roughness, and significant fatigue life improvement, are obtained simultaneously. In other words, STRB can be implemented as a mixed burnishing process.

The main purpose of this study is to assess the possibilities of STRB as a mixed burnishing process for improving SI and fatigue life of rotational components made of 2024-T3 high-strength Al alloy. An extensive study of the influence of process parameters on roughness, microhardness, residual stresses, and fatigue life was conducted using an experimental approach.

2 Experiment

2.1 Material

The chemical composition of the aluminum alloy studied is shown in Table 1. The mechanical characteristics were established at our laboratory "Testing of Metals" at the Technical University of Gabrovo. On the basis of tensile tests (at room temperature) on specimens with diameter $d = 6$ mm and base $6d$, the following material characteristics are determined: yield strength $\sigma_Y = 348$ MPa, tensile strength $\sigma_u = 501$ MPa, elongation $A_5 = 10.4\%$, and transverse contraction $\psi = 33\%$.

Table 1 2024-T3 Al alloy chemical composition

Si %	Fe%	Cu%	Mn%	Mg%	Zn%	Cr%	Al %
0.58	0.38	3.31	0.82	1.53	0.0624	0.0365	Balance

2.2 Single roller burnishing device and STRB process implementation

A special burnishing device (Fig. 2) was designed and manufactured to conduct the STRB process. The device is adapted for machining rotating components on both conventional lathes and CNC lathes. A linear law of the burnishing force F_b (400 N $\leq F_b \leq$ 1400 N) is applied using a helical spring with a stiffness of 80 N/mm. The burnishing device is equipped with five toroidal rollers with the same maximum diameter ($D = 26$ mm) but with different toroid radii of the working surface ($r = 2, 3, 4, 5,$ and 6 mm). STRB process implementation on a CNC T200 lathe is depicted in Fig. 3.
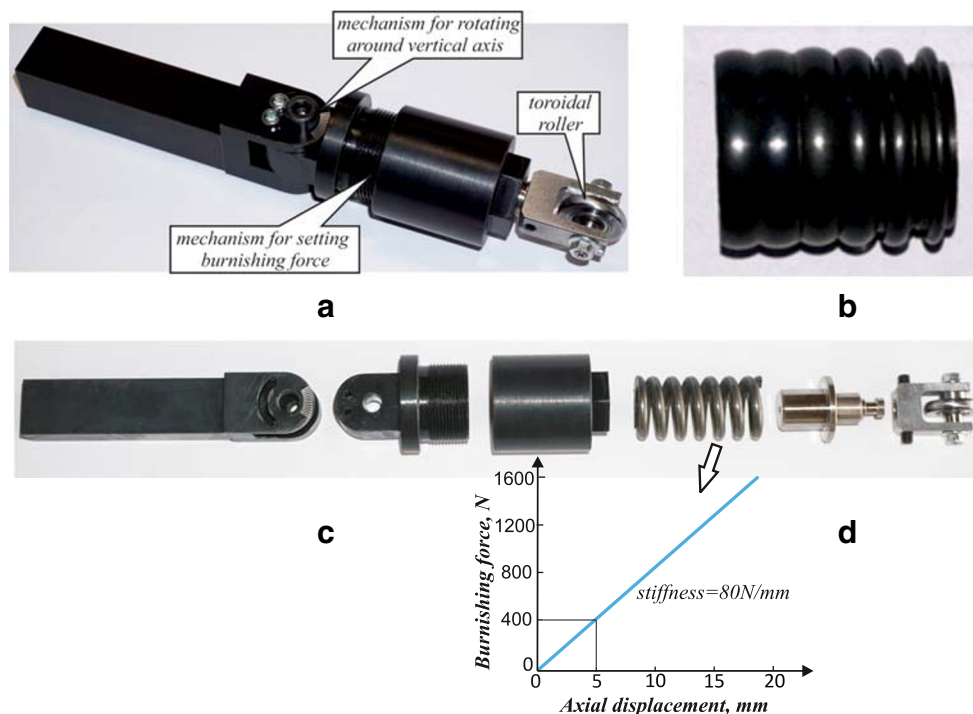
2.3 Roughness

A 3^3 type experiment was conducted to study the roughness in terms of R_a. The governing factors are outlined in Table 2. The experimental design is shown in Table 3 and is illustrated in Fig. 4. The experiment was performed on three specimens with a diameter of 22 mm and a length of 140 mm. The specimens were sequentially treated by turning, precision turning, and STRB on a CNC T200 lathe. Each specimen was clamped to one side with a chuck and supported on the other side. Precision turning and burnishing were carried out in one clamping process in the presence of a Hacut 795-H lubricant cooler. Each specimen was subjected to STRB with a different radius of the roller toroidal surface: $r = 2$ mm, $r = 4$ mm, and $r = 6$ mm. There are 12-mm-long sections to each specimen. A CCMT-120404LF KCP10 carbide cutting insert was used for precision turning and an average initial roughness of $R_a = 0.57$ μm was achieved. After the precision turning, STRB was performed on each section with a unique combination of F_b and f per the experimental design. The burnishing velocity was kept constant at $v = 63$ m/min. The three specimens were then divided into separate pieces to measure the final roughness.

The surface roughness R_a in the axial direction was measured using a Mitutoyo Surftest-4. R_a was measured along three generatrices 120° apart and then averaged to obtain a final value of R_a. Using QStatLab [27], regression analysis was conducted, and a regression model predicting the roughness was established. On this basis, the factors affecting roughness were studied and optimized using a genetic algorithm [27]. As a result, the optimum values of r, F_b, and f were established, as well as the minimum value of the roughness.

2.4 Microhardness

The same specimens in the roughness study were used to study the surface microhardness. The $HV_{0.05}$ microhardness measurements were performed using a ZHVμ Zwick/Roell microtester. For each experimental point, the surface

Fig. 2 STRB device: **a** general view; **b** toroidal deforming rollers set; **c** explode view; **d** characteristic of the helical spring

2.5 Residual stresses

The X-ray diffraction analysis determined both surface hoop σ_t^{res} and axial σ_z^{res} residual stresses in cylindrical specimens with a diameter of $d = 20$ mm and length of 30 mm. Different conditions were applied to each specimen to make a comparative assessment of the residual stresses. The STRB parameters of the specimens are shown in Table 4. The burnished

microhardness was obtained as the arithmetic mean of ten measurements within the area of the respective specimen section.

specimens were treated with the same feed rate and burnishing velocity, $f = 0.05$ mm/rev and $v = 63$ mm/min, respectively.

The X-ray diffraction measurements were performed at the Czech Technical University in Prague and carried out on a vertical θ/θ X'Pert PRO MPD diffractometer with a pinhole collimator 0.5×1.0 mm^2 in the primary beam. The specimens were positioned at the required locations by combining a versatile positioning system with six degrees of freedom and laser triangulation for precise surface position determination with an accuracy of approximately ± 5 μm. Since the effective penetration depth of the CrKα radiation into the investigated alloy was only approximately 8 μm, a 2D stressed state was assumed, and the "sin2ψ" method with a least-squares fitting procedure was used to evaluate the {311} planes for the
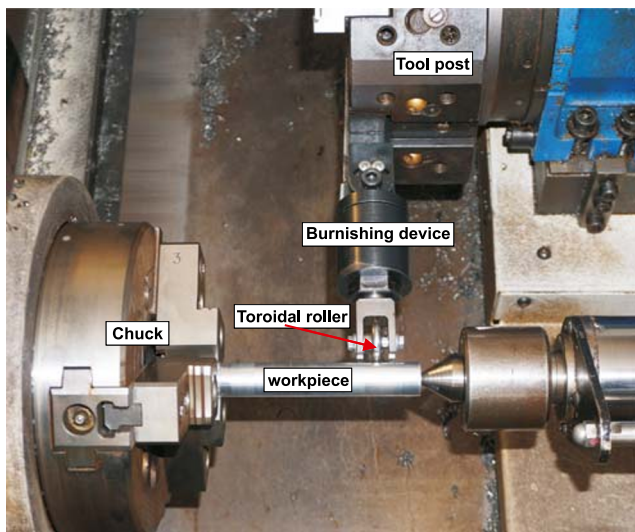

Fig. 3 STRB implementation on a CNC T200 lathe

Table 2 Governing factors and their level

Governing factors	Levels	
	Natural	Coded
Roller toroid radius (r, mm) x_1	2	− 1
	4	0
	6	+ 1
Burnishing force (F_b, N) x_2	400	− 1
	850	0
	1200	+ 1
Feed rate (f, mm/rev) x_3	0.05	− 1
	0.08	0
	0.11	+ 1

Table 3 Experimental design and results

No.	x_1	x_2	x_3	R_a, μm
1	−1	−1	−1	0.442
2	−1	−1	0	0.492
3	−1	−1	1	0.592
4	−1	0	−1	0.437
5	−1	0	0	0.631
6	−1	0	1	0.706
7	−1	1	−1	0.457
8	−1	1	0	0.465
9	−1	1	1	0.692
10	0	−1	−1	0.118
11	0	−1	0	0.134
12	0	−1	1	0.147
13	0	0	−1	0.113
14	0	0	0	0.172
15	0	0	1	0.178
16	0	1	−1	0.451
17	0	1	0	0.412
18	0	1	1	0.370
19	1	−1	−1	0.162
20	1	−1	0	0.317
21	1	−1	1	0.279
22	1	0	−1	0.148
23	1	0	0	0.260
24	1	0	1	0.321
25	1	1	−1	0.397
26	1	1	0	0.463
27	1	1	1	0.557

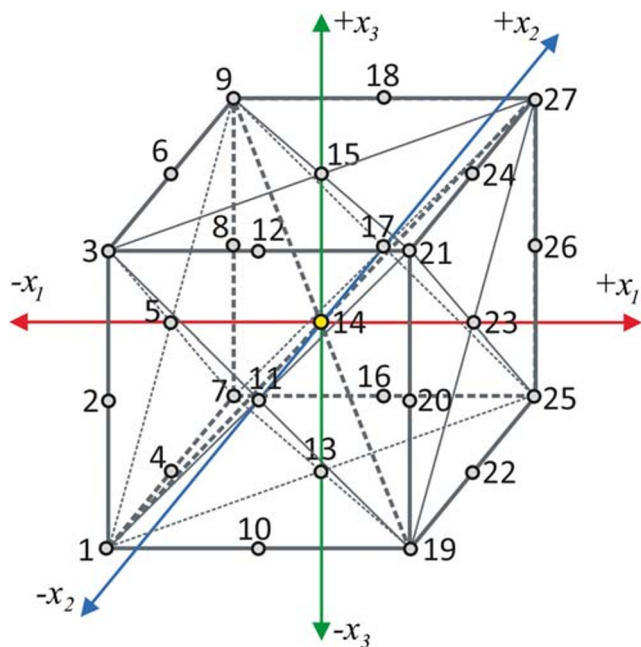**Fig. 4** Experimental design

filtered CrKα radiation with the maximum at $2\theta \approx 139.5$ °. Diffraction profiles were fitted by the Pearson VII function, and lattice deformations were calculated. In the generalized Hooke's law, the Winholtz and Cohen method and X-ray elastic constants $s_1 = 489 \times 10^{-6}$ MPa^{-1} and $\frac{1}{2}s_2 = 19.05 \times 10^{-6}$ MPa^{-1} were applied. Parameters of the X-ray experiment were as follows: 2θ range of 134–144°, 2θ step of 0.4°, tilt defined by $\sin 2\psi = 0$, 0.15, 0.3, 0.45, and 0.6 of both positive and negative values of angle ψ.

2.6 Fatigue behavior study

2.6.1 Purpose of the study

The goal of this study was to compare the conventional fatigue limits of two groups of samples. The first group was processed only by cutting, and the second was treated by STRB with optimal process parameters under a minimum roughness criterion.

2.6.2 Details of the study

To obtain a comparative assessment of the two groups of samples, S-N curves were constructed based on three-point rotating bending fatigue tests ($R = -1$) at a frequency of 50 Hz. The fatigue tests were conducted on a UBM testing machine. The rotating load magnitude P and hence the bending moment M were controlled through a lever system. The S-N curves were built as each sample was tested for each stress amplitude. Each fatigue test was ended after the complete destruction of the sample or if a maximum number of cycles N_{max} in the range of $(10.1 \div 14.3) \times 10^6$, corresponding to the so-called limited fatigue strength, was achieved. If significant scattering was present, the tests were repeated with the appropriate amplitude as needed. For non-ferrous alloys, including the 2024-T3 Al alloy, the conventional fatigue limit is adopted, relating to 2×10^8 base number of cycles. The intersection between a tangent line at the point on the S-N curve corresponding to the maximum number of cycles N_{max} and a vertical line at 2×10^8 cycles defines the search conventional fatigue limit.

2.6.3 Specimen preparation

Hourglass-shaped fatigue specimens were used in the experiment, as shown in Fig. 5a. The specimens were manufactured on a CNC Okuma lathe (Fig. 5b). The turning was carried out using CCMT-120404LF KCP10 cutting inserts at the following manufacturing parameters: feed rate of 1.0 rev/mm, the velocity of 60 m/min, and cutting depth of 0.5 mm. The first group of samples was processed only by turning. Using the developed burnishing device, the second group was

Int J Adv Manuf Technol (2020) 111:3559–3570

Table 4 X-ray specimen specification

Specimen number	Type of finishing	Roller toroid radius, r, mm	Burnishing force, F_b, N	Number of passes, n
1	Precision turning (reference condition)	-	-	-
2	STRB	4	800	1
3		4	400	1
4		4	1300	1
5		2	800	1
6		6	800	1
7		4	800	6

subjected to STRB with optimal process parameters under a minimum roughness criterion.

3 Results and discussion

3.1 Roughness

3.1.1 Analysis of variance

The experimental results are shown in Table 3. Analysis of variance (ANOVA) was conducted in order to study the factor influence (Fig. 6), using QStatLab software [27]. The outcomes are shown in Table 5. The most significant factor (see Fig. 6a) is x_1 (roller toroidal radius), and the most insignificant factor is x_3 (feed rate). The minimum radius size leads to the highest roughness, while the average level ($r = 4$ mm) minimizes the roughness. Obviously, with increasing the burnishing force and feed, the resulting roughness increases. Completely expected, the interaction between the factors x_1 and x_2 (roller toroidal radius and burnishing force) is the most significant (see Fig. 6b), since a correlation exists between the respective combination of x_1 and x_2, on the one hand, and the area of the contact zone and the depth of penetration, on the other hand. In turn, the area of the contact zone and the depth of penetration of the deforming roller correspond to a certain surface pressure, which is defined by the radius-burnishing force combination.

3.1.2 Regression model

Given the experimental design, the regression model of the objective function YRa, which predicts the roughness, was chosen to be a second-order polynomial:

$$Y_{R_a} = 0.200 - 0.112x_1 + 0.088x_2 + 0.062x_3 + 0.202x_1^2 + 0.056x_2^2 - 0.007x_3^2 + 0.048x_1x_2 + 0.002x_2x_3 - 0.017x_1x_3 - 0.005x_1x_2x_3 \quad (1)$$

The dependence between coded x_1 and natural $\widetilde{x}_i$ factors is:

$$x_i = \left(\widetilde{x}_i - \widetilde{x}_{0,i}\right)/\lambda_i \quad (2)$$

where $\lambda_i = \left(\widetilde{x}_{\min,i} - \widetilde{x}_{\min,i}\right)/2$, $\widetilde{x}_{0,i}$, $\widetilde{x}_{\min,i}$, and $\widetilde{x}_{\min,i}$ are, respectively, average and upper and lower levels of the ith natural factor. After substituting (2) in (1), the expression of roughness in natural variables is obtained.

3.1.3 Study of the model predicting the roughness obtained

The influence of the factors on the objective function YRa is illustrated on the graphs of representative sections of the hyper-surface of the model (1) with different
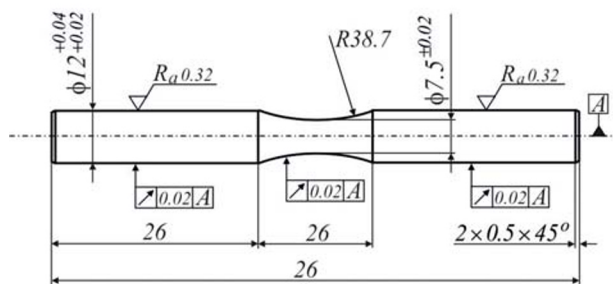

Fig. 5 Fatigue specimen: **a** sizes; **b** manufacturing on a CNC Okuma lathe

Springer

Fig. 6 Outcomes from ANOVA:
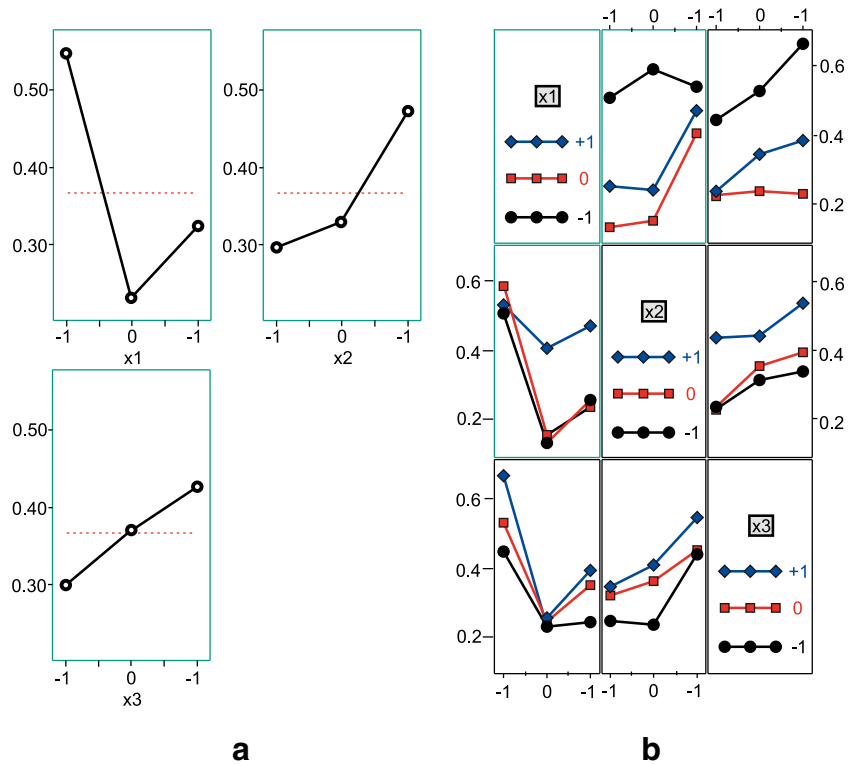**a** main effects; **b** interactions
between the governing factors

a   b

Table 5 ANOVA outcomes

Analysis of variance (ANOVA) for roughness obtained R_a- (x_1; x_2; x_3)

Symbol	Name	Number of levels				Levels	
x_1	x_1	3			-1	0	1
x_2	x_2	3			-1	0	1
x_3	x_3	3			-1	0	1
Source	Amounts	Degree of freedom		Dispersion	F	P	
x_1	0.46820	2		0.23410	29.07566	0.00000	
x_2	0.15794	2		0.07897	9.80844	0.00108	
x_3	0.06961	2		0.03480	4.32258	0.02753	
Remainder	0.16103	20		0.00805			
Sum	0.85677	26					

Residual mean square deviation (RMSD) = 0.08973; R^2 = 0.81205; R^2 (adj) = 0.75567

Confidence intervals for the average value at each factor level: confidence intervals are based on the standard deviation for each factor level

Factor	Level	Number	Mean	Dispersion	95% confidence interval
x_1	-1	9	0.54600	0.01204	$0.4616 \leq 0.5460 \leq 0.6304$
	0	9	0.23278	0.01874	$0.1276 \leq 0.2328 \leq 0.3380$
	1	9	0.32267	0.01779	$0.2201 \leq 0.3227 \leq 0.4252$
x_2	-1	9	0.29811	0.03077	$0.1633 \leq 0.2981 \leq 0.4329$
	0	9	0.32956	0.04709	$0.1628 \leq 0.3296 \leq 0.4964$
	1	9	0.47378	0.00950	$0.3988 \leq 0.4738 \leq 0.5487$
x_3	-1	9	0.30278	0.02575	$0.1794 \leq 0.3028 \leq 0.4261$
	0	9	0.37178	0.02653	$0.2466 \leq 0.3718 \leq 0.4970$
	1	9	0.42689	0.04612	$0.2618 \leq 0.4269 \leq 0.5920$

hyper-planes (Fig. 7). The roughness R_a as a function of the roller toroid radius r and feed rate f is shown in Fig. 7a–c, when the burnishing force F_b is fixed at the lower, middle, and upper levels, respectively. The increase in feed rate leads to a deterioration of R_a, and this trend is most pronounced when the burnishing force is highest (Fig. 7c). Figure 7d–f show predictions of the roughness R_a as a function of the feed rate f for different values of the burnishing force F_b and radius r. The burnishing force in the $850 \leq F_b \leq 1300$ N interval at all feed rates cannot achieve the desired roughness. A larger radius leads to more scattering of the roughness (Fig. 7d–f). The smallest roughness obtained for $r = 2$ mm is greater than all predicted values of R_a, corresponding to $r = 4$ mm and $r = 6$ mm, with the exception of the combination of $r = 6$ mm and $F_b = 1300$ N. Therefore, it is impractical to carry out the process with the roller toroid radius $r = 2$ mm.

For all values of the burnishing force F_b and feed rate f, the roughness function is nonlinear (Fig. 7g–i) depending on the radius. The roughness minimizes at $r \approx 4$ mm for $F_b = 1300$ N,

at $r \approx 4.5$ mm for an F_b interval of $(870 \div 1075)$ N, and at $r \approx 5$ mm for an F_b interval of $(400 \div 625)$ N.

3.1.4 Process optimization under a minimum roughness criterion

The careful study of the roughness model (see Fig. 7) shows that the slowest feed rate provides minimum roughness for all combinations of r and F_b. 3D visualization of the roughness model when $f = 0.05$ mm/rev is depicted in Fig. 8a. The optimization of the model (1) under a minimum roughness criterion was conducted by QStatLab using a genetic algorithm (Fig. 8b). The number of iterations was 2500. The dependence of the minimum surface roughness found on the iteration number is depicted in Fig. 9. Table 6 shows the governing factors of this optimization in coded form and natural coordinates minimizing the roughness function: $Y_{Ra} \rightarrow$ min. The extra tests with process parameters $r = 5$ mm, $F_b = 43$ N, and $f = 0.05$ mm/rev (which are nearly optimal conditions from Table 6) provided an average roughness of $R_a = 0.1$ μm.
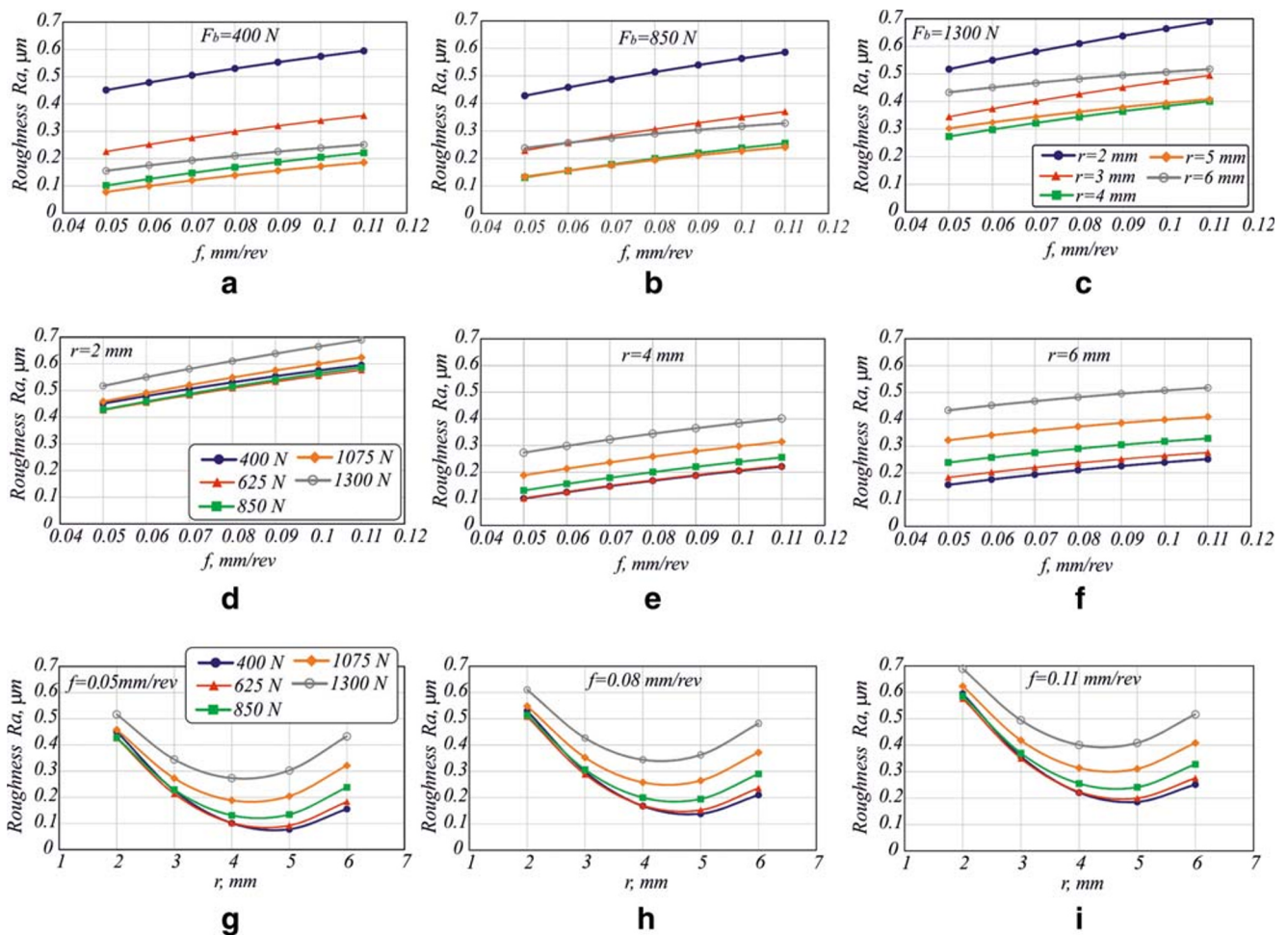

Fig. 7 3D graphs, representing sections of the hyper-surface of the roughness obtained model with different hyper-planes
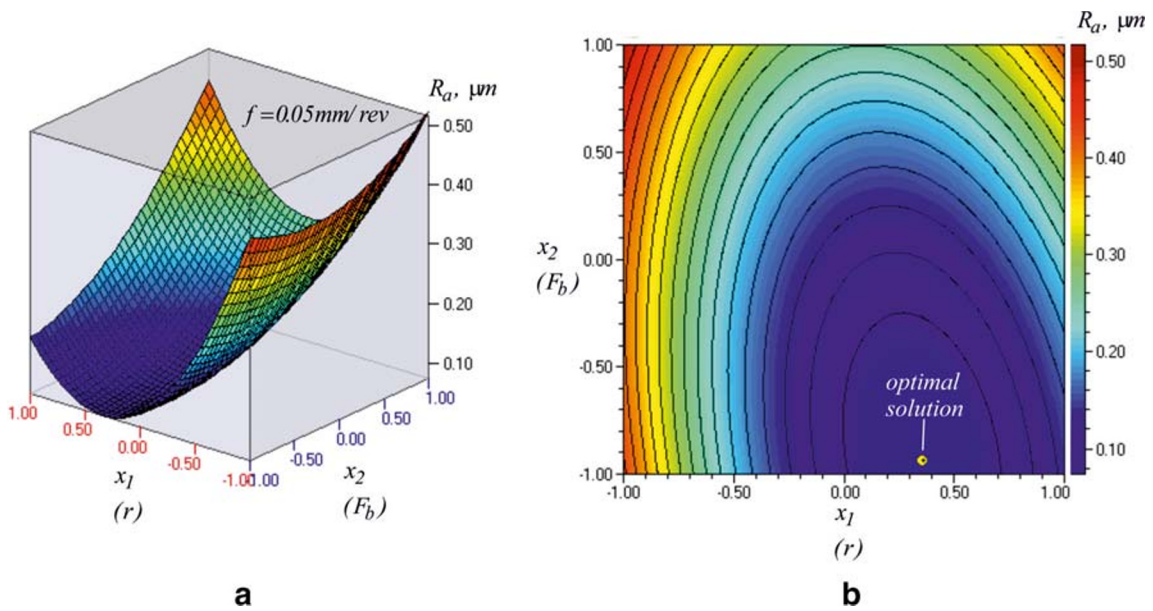
Fig. 8 Dependence of the roughness on the radius and burnishing force: **a** 3D visualization; **b** optimization results

3.2 Surface microhardness

The average values of the measured surface microhardness $HV_{0.05}$ for all 27 specimens are summarized in Fig. 10a–c. The difference between the largest and the smallest average value is 10.3 units, which shows that there are no clear trends regarding the governing factors for the surface microhardness. The surface microhardness for each sample varies within narrow limits. The scattering is 3.3 units at $r = 2$ mm, 4.7 units at $r = 4$ mm, and 2.8 units at $r = 6$ mm. These scattering values are within the statistical error of the measured microhardness. Therefore, the STRB of 2024-T3 aluminum alloy specimens provides a homogeneous surface in terms of surface microhardness. The initially measured microhardness was $HV_{0.05}^{init} = 117$. The optimum process parameters under a minimum roughness criterion achieved a surface microhardness $HV_{0.05} = 161$. Therefore, the surface microhardness increase coefficient $k_{HV0.05}$ is

$$k_{HV_{0.05}} = \frac{HV_{0.05} - HV_{0.05}^{init}}{HV_{0.05}^{init}} \times 100\% = 37.6\%.$$

3.3 Residual stresses

The X-ray diffraction analysis results are shown in Fig. 11 for the surface axial σ_z^{res} and hoop σ_t^{res} residual stresses in the examined specimens (see Table 3) and the following comments can be made:

- Taking into account the X-ray measurement error, both types of residual stresses in specimen 1, processed only by turning (reference condition), are negligibly small. Significant compressive axial and hoop residual stresses were measured in the samples treated via STRB. This proves the studied process yields a favorable macro-effect in the 2024-T3 Al alloy.

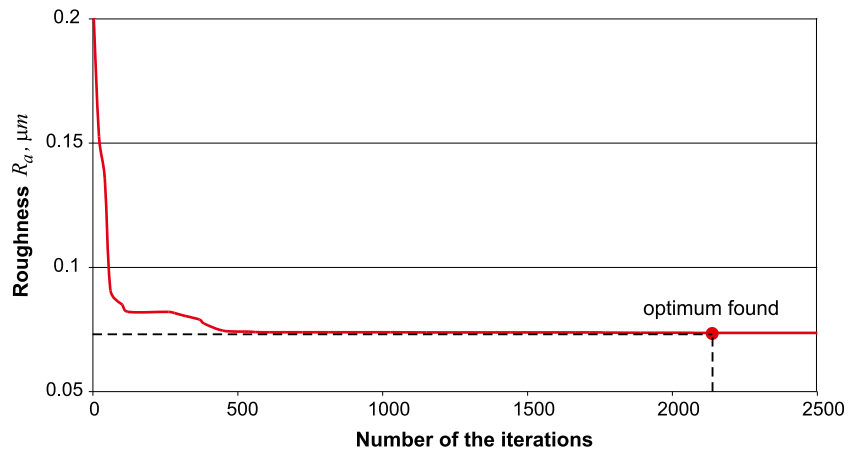**Fig. 9.** Dependence of the minimum surface roughness found on the iteration number

Table 6 Optimal values of the governing factors minimizing the roughness obtained

	Roller toroid radius		Burnishing force		Feed rate		Roughness
	Coded, x_1	Natural (r, mm)	Coded, x_2	Natural (F_b, N)	Coded, x_3	Natural $(f, \text{mm/rev})$	R_a, μm
	0.3572	4.7144	− 0.9342	429.60	− 1.0000	0.05	0.074

- Regardless of the combination of r and Fb, the axial residual stresses σ_z^{res} are larger than the hoop stresses σ_t^{res} in all specimens subjected to STRB.
- Specimens 2, 3, and 4 were burnished with the same radius (r = 4 mm), but with different burnishing forces. Taking into account the X-ray diffraction technique error characteristic ($\Delta\sigma = 2 \div 33\ MPa$), the measured axial and hoop residual stresses are nearly equal and do not show a
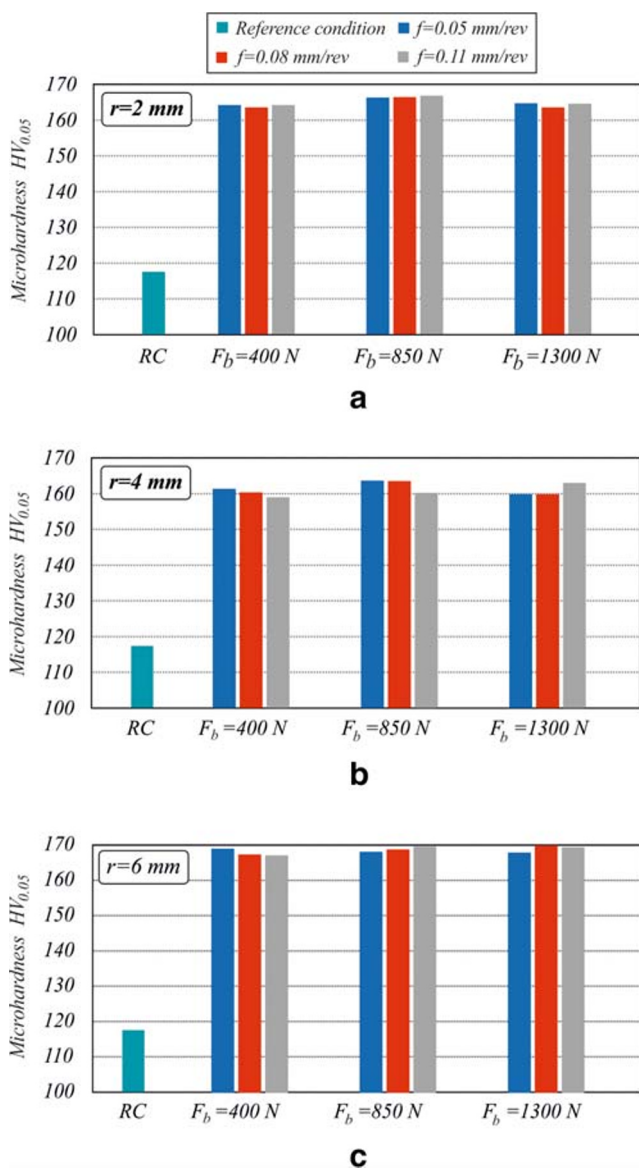
pronounced dependency on the burnishing force. The axial residual stresses are the largest in specimen 4 ($\sigma_z^{res} = -411 MPa$), treated with the largest burnishing force (F_b = 1300 MPa), and the smallest in specimen 2 ($\sigma_z^{res} = -386 MPa$), treated with the average value of the burnishing force (F_b = 800 MPa). The largest value of hoop residual stress is measured in specimen 3 ($\sigma_t^{res} = -189 MPa$), burnished with the least burnishing force.

- Specimens 2, 5, and 6 were burnished with the same burnishing force (F_b = 800 N) but with different radii. The measured axial and circumferential residual stresses in this specimen group show that, with increasing radius, both types of surface residual stresses increase in magnitude. The largest axial ($\sigma_z^{res} = -432 MPa$) and hoop ($\sigma_t^{res} = -181 MPa$) residual stresses were measured in specimen 6, which was burnished with the largest radius (r = 6 mm), and the smallest residual stresses were measured in specimen 5, treated with the smallest radius (r = 2 mm).

- As in other static burnishing processes, the roller toroid in the process studied is much larger compared to the feed rate values. As a consequence, in the direction of a generatrix from the workpiece cylindrical surface, the contact zones overlap between the roller and the treated surface. As a result, even within a pass, the points from the surface layers are subjected to cyclic loading. For a workpiece with a specific material and diameter, the cyclic loading depends on the roller geometry, feed rate, and depth of penetration (a function of F_b). Therefore, the different combinations of r and F_b cause different characteristics of strain hardening, the effect of which is expressed in the distribution of the axial and circumferential residual stresses on the surface and at a particular depth.

- The results obtained for specimen 7, which was treated as specimen 2 but with six passes (n = 6), confirm the significance of the number of passes as a factor in creating a more pronounced zone with useful compressive residual stresses and, hence, increasing fatigue life.

Fig. 10 Surface microhardness generalized results

3.4 Fatigue strength

The empirically derived S-N curves are shown in Fig. 12. For the specimens treated only by turning (reference condition), a

Fig. 11 Surface axial σ_z^{res} and hoop σ_t^{res} residual stresses
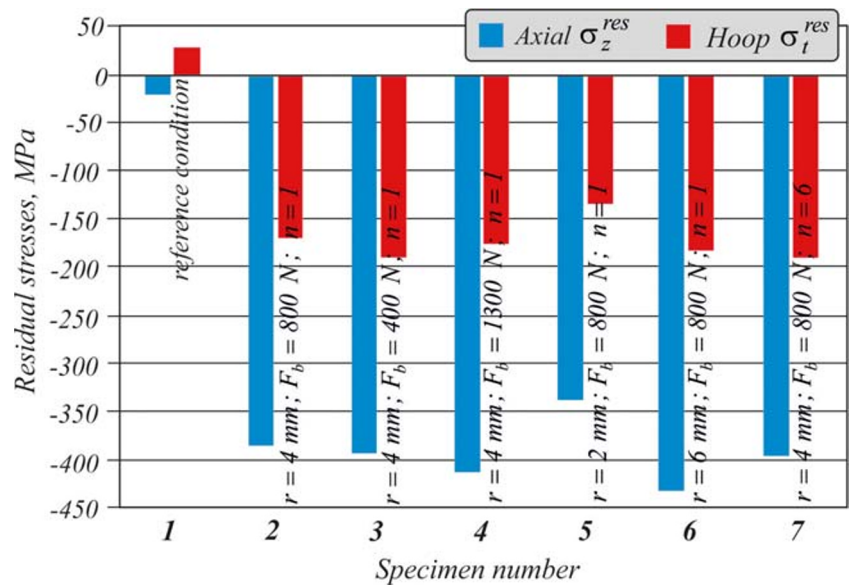
conventional fatigue limit is σ_{-1} = 185 MPa, and for those subjected to STRB with optimum process parameters under a minimum roughness criterion, the conventional fatigue limit is σ_{-1} = 250 MPa. Therefore, the STRB implementation with parameter values providing minimum roughness increases the conventional fatigue limit by 35.1% and the fatigue life by more than 2000 times in comparison with the reference condition.

4 Conclusions

The effect of STRB with different combinations of process parameters on SI and fatigue behavior of 2024-T3 Al alloy specimens was established through a

comprehensive experimental study. The following conclusions can be made.

- Through a full factorial experiment, regression analysis, and model optimization, the following optimal STRB process parameters were established under a minimum roughness criterion: $r \approx 5$ mm, F = 430 N, and f = 0.05 mm/rev. Using these parameters, the average roughness was R_a = 0.1 μm.
- Compared to the reference condition, it was proven that the STRB provides a relatively homogeneous surface in terms of surface microhardness. The surface microhardness increase coefficient $k_{HV0.05}$ was 37.6% when the STRB was implemented with the optimal parameters.

Fig. 12 S-N curves—comparison between the reference condition and STRB with optimal parameters under minimum roughness criterion
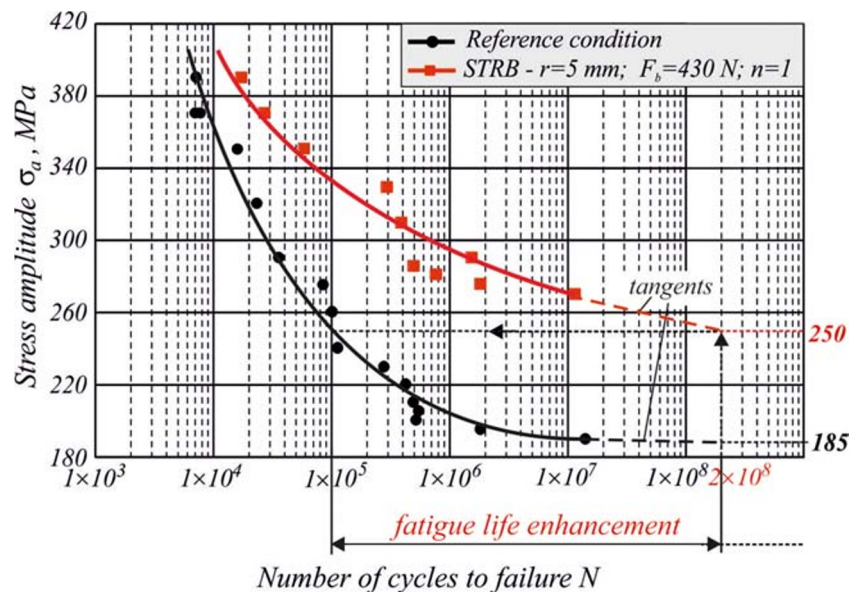
- The X-ray stress analysis results confirm the effectiveness of STRB of 2024-T3 Al alloy to introduce significant surface residual compressive axial and hoop stresses. It was proved that STRB with six passes introduces greater magnitudes of surface residual stresses.
- The STRB implementation with optimal parameters under a minimum roughness criterion increases the conventional fatigue limit by 35.1%, and the fatigue life enhances more than 2000 times in comparison with the reference condition.
- Based on the results obtained, STRB of 2024-T3 Al alloy can be successfully implemented as a mixed burnishing process with the following parameters: $r = 5$ mm, $F_b = 430$ N, and $f = 0.05$ mm/rev. This provides a mirror-finish surface ($R_a = 0.1$ μm) and an increase in fatigue life by more than 2000 times compared to the reference condition.
- This technique can be used in automotive, aircraft, oil, gas industries, machine construction, and treatment of external rotary surfaces of axles, shafts, collar pins, piston rods, valve stems, and others. For example, a typical application for aluminum shafts is for linear bearings.

References

1. Maximov JT, Duncheva GV, Anchev AP, Ichkova MD (2019) Slide burnishing—review and prospects. Int J Adv Manuf Technol 104:785–801
2. Ecoroll Catalogue Tools and solutions for metal surface improvement (2006) Ecoroll Corporation Tool Technology USA
3. Abrão AM, Denkena B, Köhler J, Breidenstein B, Mörke T (2014) The influence of deep rolling on the surface integrity of AISI 1060 high carbon steel. Proc CIRP 13:31–36
4. Abrão AM, Denkena B, Köhler J, Breidenstein B, Mörke T (2015) The inducement of residual stress through deep rolling of AISI 1060 steel and its subsequent relaxation under cyclic loading. Int J Adv Manuf Technol 79(9-12):1939–1947
5. Zhang P, Lindemann J, Ding WJ, Leyens C (2010) Effect of roller burnishing on fatigue properties of the hot-rolled Mg–12Gd–3Y magnesium alloy. Mater Chem Phys 124:835–840
6. Fouad Y, Mhaede M, Wagner L (2010) Effect of mechanical surface treatment on fatigue performance of extruded ZK60 alloy. Fatigue Fract Eng Mater Struct 34:403–407
7. Wagner L, Mhaede M, Wollmann M, Altenberger I, Sano Y (2011) Surface layer properties and fatigue behavior in Al 7075-T73 and Ti-6Al-4V. Comparing results after laser peening; shot peening and ball-burnishing. Int J Str Integr 2(2):185–199
8. Gomez-Gras G, Travieso-Rodriguez JA, Jerez-Mesa R (2015) Experimental characterization of the influence of lateral pass width on results of a ball burnishing operation. Proc Eng 132:686–692
9. Chomienne V, Valiorgue F, Rech J, Verdu C (2016) Influence of ball burnishing on residual stress profile of a 15-5PH stainless steel. CIRP J Manuf Sci Technol 13:90–96
10. Lindemann J, Glavatskikh M, Leyensl C, Oehring M, Appel F (2007) Influence of mechanical surface treatments on the high cycle fatigue performance of gamma titanium aluminides Ti-2007. Science and Technology, The Japan Institute of Metals 1703-1706
11. López de Lacalle LN, Lamikiz A, Sánchez JA, Arana JL (2007) The effect of ball burnishing on heat-treated steel and Inconel 718 milled surfaces. Int J Adv Manuf Technol 32:958–968
12. Yuan X, Sun Y, Li C, Liu W (2017) Experimental investigation into the effect of low plasticity burnishing parameters on the surface integrity of TA2. Int J Adv Manuf Technol 88:1089–1099
13. Frihat MH, Al Quran FMF, Al-Odat MQ (2016) Experimental Investigation of the Influence of Burnishing Parameters on Surface Roughness and Hardness of Brass Alloy. J Mater Sci Eng 5(1):1–4
14. Malleswara Rao JN, Chenna Kesava RA, Kama KPV (2011) The effect of roller burnishing on surface hardness and surface roughnes on mild steel specimens. Int J Appl Eng Res 4:777–785
15. Kurkute V, Chavan ST (2018) Modeling and optimization of surface roughness and microhardness for roller burnishing process using response surface methodology for aluminum alloy 63400. Proc Manuf 20:542–547
16. Kiran AP, Pragnesh KB (2015) Surface roughness prediction for roller burnishing of 6061Al alloy using response surface method. Int J Sci Eng Res 6(3):636–640
17. Othman OA, Basha M, Wagner L (2016) Optimizing the process parameters and investigating the influence of shot peening and roller burnishing on surface layer properties and fatigue performance of AI 6061 T4. Sohag J Sci 1(1):65–72
18. Hemanth S, Harish A, Nithin Bharadwaj R, Abhishek BB (2018) Design of roller burnishing tool and its effect on the surface integrity of Al 6061. Mater Today: Proc 5:12848–12854
19. Shankar E, Balasivanandha Prabu S, Sampath Kumar T, Stalin John MR (2018) Investigation of TiAlN coated roller burnishing on Al-(B4C)p MMC workpiece material. Mater Manuf Process 33(11):1242–1249
20. Al-Qawabena UF, Al-Qawabah SM (2013) Effect of roller burnishing on pure aluminum alloyed by copper. Industr Lubric Tribol 65(2):71–77
21. Tian Y, Shin YC (2007) Laser-assisted burnishing of metals. Int J Mach Tool Manuf 47:14–22
22. Borkar AP, Kamble PS, Seemikeri CY (2014) Surface integrity enhancement of inconel 718 by using roller burnishing process. Int J Curr Eng Technol 4(4):2595–2598
23. Hassani-Gangaraj S, Carboni M, Gnagliano M (2015) Finite element approach toward an advanced understanding of deep rolling induced residual stresses, and an application to railway axles. Mater Des 83:689–703
24. Dwivedi SP, Sharma S, Mishra RK (2014) Effects of roller burnishing process parameters on surface roughness of A356/5%SiC composite using response surface methodology. Adv Manuf 2:303–317
25. Perenda J, Trajkovski J, Zerovnik A, Prebil I (2015) Residual stresses after deep rolling of a torsion bar made from high strength steel. J Mater Process Technol 218:89–98
26. Duncheva GV, Atanasov TP (2020) Finite element modeling and optimization of the deep rolling process with a torodal roller in aluminum alloy 2024 T3. J Tech Univ Gabrovo 60:3–14
27. Vuchkov IN, Vuchkov II (2009) QStatLab Professional, v. 5.5 – statistical quality control software. User's Manual Sofia

Publisher's note Springer Nature remains neutral with regard to jurisdictional claims in published maps and institutional affiliations.